*Journal of Sound and Vibration* (2000) **233**(1), 93–118
doi:10.1006/jsvi.1999.2795, available online at http://www.idealibrary.com on IDEAL®

# PARTICLE IMPACT DAMPING

R. D. Friend and V. K. Kinra

*Department of Aerospace Engineering, Texas A&M University, Center for Mechanics of Composites, College Station, TX* 77843-3141, *U.S.A.*

(*Received* 28 *June* 1999, *and in final form* 19 *November* 1999)

Particle impact damping (PID) is a means for achieving high structural damping by the use of a particle-filled enclosure attached to the structure in a region of high displacements. The particles absorb kinetic energy of the structure and convert it into heat through inelastic collisions between the particles and the enclosure, and amongst the particles. In this work, PID is measured for a cantilevered aluminium beam with the damping enclosure attached to its free end; lead particles are used in this study. The effect of acceleration amplitude and clearance inside the enclosure on PID is studied. PID is found to be highly non-linear. Perhaps the most useful observation is that for a very small weight penalty (about 6%), the maximum specific damping capacity (SDC) is about 50%, which is more than one order of magnitude higher than the *intrinsic material damping* of a majority of structural metals (O(1%)). Driven by the experimental observations, an elementary analytical model of PID is constructed. A satisfactory comparison between the theory and the experiment is observed. An encouraging result is that in spite of its simplicity, the model captures the essential physics of PID.



## 1. INTRODUCTION

Particle impact damping (PID) is a form of impact damping in which particles of various shapes, sizes, and materials are inserted into an enclosure attached to a structure. Particle-to-enclosure collisions arise due to a clearance, $d$, between the particles and the enclosure walls. As a result of these collisions, momentum is exchanged between the structure and the particles, and kinetic energy is converted to heat. Additional energy dissipation can also occur due to frictional losses and inelastic particle-to-particle collisions. The unique aspect of PID is that high damping is achieved by absorbing the kinetic energy of the structure as opposed to the more traditional methods of damping where the elastic strain energy stored in the structure is converted to heat. Viscoelastic materials have long been used for increasing damping in structures. However, they lose their effectiveness in low- and high-temperature environments and degrade over time. Particle impact damping offers the potential for the design of an extremely robust passive damping technique with minimal impact on the strength, stiffness and weight of a structure. With a proper choice of particle materials (for example, lead, steel, or tungsten carbide), this technique is essentially independent of temperature and is very durable. Also, this technique appears to be an improvement over single-particle impact dampers that suffer from impact-induced high noise levels and surface degradations as well as high sensitivity to container size and input excitation.

Several studies have been conducted relating to the effectiveness of particle impact damping in attenuating undesirable vibrations. Papalou and Masri [1] studied the behavior of particle impact dampers in a horizontally vibrating single-degree-of-freedom

0022-460X/00/210093 + 26 $35.00/0 

(s.d.o.f.) system under random excitation. They studied the influence of mass ratio, particle size, container box dimensions, excitation levels, and direction of excitation. Damper container design criteria were provided for optimal efficiency based upon reduction in system response. Cempel and Lotz [2] used a simplified energy approach to measure the influence of various particle packing configurations on the damping loss factor of a s.d.o.f. system under horizontal forced vibration. Popplewell and Semergicil [3] observed that a plastic "bean bag" filled with lead shot exhibited greater damping effectiveness and "softer" impacts than a single lead slug of equal mass. The aforementioned studies were confined to frequencies at or below 20 Hz. Panossian [4, 5] studied non-obstructive particle damping in the modal analysis of structures at a higher frequency range of 300–5000 Hz. This method consists of drilling small diameter cavities at appropriate locations in a structure (for example, turbine blades) and partially or fully filling the holes with particles of different materials and sizes (steel shot, tungsten powder, nickel powder, etc.). Significant decrease in structural vibrations was observed even when the holes were completely filled with particles and subjected to a pressure as high as 240 atms.

The primary objective of this work is to measure non-linear particle impact damping in the context of free vibration of a cantilevered beam in the vertical plane. Lead powder was used in this study. The effect of gravity, vibration amplitude, and particle fill ratio (or clearance) on the structural damping were studied. The secondary objective is to construct an elementary analytical model to predict particle impact damping. In spite of its deceptive simplicity, the model was found to be surprisingly effective in capturing the essential physics of particle impact damping. A satisfactory agreement between theory and experiment was observed.

## 2. THEORETICAL ANALYSIS

### 2.1. EQUATIONS OF MOTION

In this section an elementary model of particle impact damping is developed. A schematic of the beam and the damping enclosure that contains the particles is drawn to scale in Figure 1(a). The beam is idealized as a standard Euler–Bernoulli beam (Figure 1(b)). The well-known fourth order partial differential equation of motion is used to describe its motion [6]. Neglecting its rotary inertia, the enclosure is idealized as a point mass attached to the tip of the beam; in the following we shall refer to it as the end mass, $m_e$. The beam is assumed to vibrate in its fundamental mode, $\phi(x; m_e)$. The mode shape is normalized in such a manner that $\phi(L; m_e) = 1$ [7]. Let $\omega$ be the circular frequency of the fundamental mode, and $\psi_b$ the *intrinsic material damping* of the beam material.

We will find it convenient to reduce the continuous beam to an equivalent s.d.o.f. system (see Figure 1(c)) [8]. The point $x = L$ is an obvious choice for this reduction. The reduced mass of the beam and the end mass is given by

$$M = m_e + \gamma \int_0^L [\phi(x; m_e)]^2 \, dx, \tag{1}$$

where $\gamma$ is the mass per unit length of the beam. Often, $M$ is referred to as the primary mass of the equivalent s.d.o.f. system. The reduced stiffness of the beam at $x = L$ is given by

$$K = EI \int_0^L [\phi''(x; m_e)]^2 \, dx, \tag{2}$$

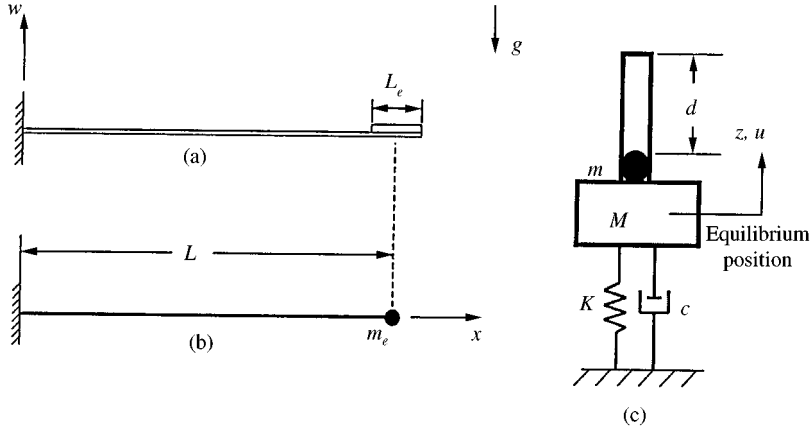


Figure 1. (a) A schematic of the beam and enclosure (drawn to scale). (b) A model of the beam with end mass, $m_e$. (c) The equivalent single-of-freedom (s.d.o.f.) system. The displacement, $u$, of the mass, $M$, is measured from its equilibrium position with the particle mass, $m$, resting on the bottom of the enclosure. The origin of the co-ordinate $z$ is also located at the equilibrium position of $M$.

where $\phi'' = \mathrm{d}^2\phi/\mathrm{d}x^2$, and $EI$ is the flexural stiffness of the beam. The reduced damping coefficient of the beam is given by

$$c = \frac{\psi_b}{2\pi}\sqrt{KM}. \tag{3}$$

Then, the damping ratio, $\zeta = c/c_{cr} = c/(2\sqrt{KM}) = \psi_b/4\pi$. Since we use the exact mode shape in computing $M$ and $K$, the undamped natural frequency of the equivalent s.d.o.f. system, $\sqrt{K/M}$, is *exactly* equal to the undamped natural frequency of the first mode of the beam, $\omega$; the same is true for the damped natural frequency. Moreover, for the beam used in this study, the damped natural frequency may be approximated by its undamped natural frequency, i.e., $\omega_d \approx \omega$. To give the reader a feel for the numerical values involved, for the particular beam studied in this work, the reduced mass of the beam is 24·1% of its actual mass. (See the Experimental Procedures section for a description of the beam.) Moreover, $K/(3EI/L^3) = 1{\cdot}01$, i.e., the reduced stiffness of the vibrating beam is very nearly equal to its static stiffness. ($3EI/L^3$ is the well-known static stiffness of a cantilevered beam loaded at its tip, $x = L$.)

In most vibration problems the mass of the beam remains constant. Therefore, the static deflection due to the weight of the beam also remains constant and is neglected. For the case at hand, there are times when the particles move in contact with the beam, and at other times they move separately from the beam. It is assumed that all the particles move as a lumped mass, $m$, i.e., the relative motion between the particles is neglected. This makes the end mass, $m_e$, a two-valued function which, in turn, makes $\phi(x; m_e)$, $M$, $K$, and $\omega$ two-valued functions as well. Moreover, the static deflection due to gravity is no longer a constant. Therefore, the static deflection must be taken into account in the analysis of the problem. With this observation, the analogy between the continuous beam (Figure 1(b)) and its equivalent discrete s.d.o.f. system (Figure 1(c)) is complete.

Let the schematic in Figure (1c) represent the static equilibrium position of the *primary mass including the particles*. We take the equilibrium position as the origin of a co-ordinate $z$; the displacement of the primary mass, $u$, is also measured from this point. The motion of

the s.d.o.f. system is governed by

$$M\frac{d^2u}{dt^2} + c\frac{du}{dt} + Ku = F(t)$$

or

$$\frac{d^2u}{dt^2} + 2\zeta\omega\frac{du}{dt} + \omega^2 u = \frac{F(t)}{M}, \tag{4}$$

where $F(t)$ is a two-valued (piecewise constant) function of time: $F(t) = 0$ when the particles are moving separately from the beam; $F(t) = -mg$, when the particles are in contact with beam, where $g$ is the acceleration due to gravity. We consider these two cases separately.

2.1.1. *State* 1: *the particles move in contact with the beam*

Subscript $(\ )_1$ will be used to denote all quantities in State 1. Let $m_{encl}$ be the mass of the enclosure and the beam of length $L_e/2$. Then, the end mass, $m_{e1} = m_{encl} + m$. Let $\phi_1$, $M_1$, $K_1$, $\omega_1$, and $F_1 = -mg$ be the corresponding quantities. Let $u_0$ and $v_0$ be, respectively, the displacement and velocity of $M_1$ at any time $t$ taken to be zero ($t = 0$). For $t > 0$, the motion is given by

$$u_1(t) = \left[u_0\cos(\omega_1 t) + \left(\frac{v_0}{\omega_1} + \frac{\psi_b}{4\pi}u_0\right)\sin(\omega_1 t)\right]e^{(-\psi_b/4\pi)\omega_1 t}. \tag{5}$$

2.1.2. *State* 2: *the particles move separately from the beam*

Subscript $(\ )_2$ will be used to denote all quantities in State 2. Then the end mass is $m_{e2} = m_{encl}$. Let $\phi_2$, $M_2$, $K_2$, $\omega_2$, and $F_2 = 0$ be the corresponding quantities. Once again, let $u_0$ and $v_0$ be, respectively, the displacement and velocity of $M_2$ at time $t = 0$. For $t > 0$, the motion is given by

$$u_2(t) = \frac{mg}{K_2} + \left[\left(u_0 - \frac{mg}{K_2}\right)\cos(\omega_2 t) + \left(\frac{v_0}{\omega_2} + \frac{\psi_b}{4\pi}\left(u_0 - \frac{mg}{K_2}\right)\right)\sin(\omega_2 t)\right]e^{(-\psi_b/4\pi)\omega_2 t}, \tag{6}$$

where the term, $mg/K_2$, is recognized as the static deflection due only to the mass of the particles, $m$.

## 2.2. ENERGY DISSIPATED AND DAMPING

Next, we derive an expression for the energy dissipated during an impact between the particles ($m$) and the primary mass ($M_2$). It is envisioned that, after an impact, individual particles travel at different velocities. However, it is assumed that all particles move as a single particle, and that its motion is confined to the $z$ direction. In reality (considering the first impact of the particles with the ceiling, for example), the particles belonging to the top layer impact the ceiling first, the particles belonging to the second layer impact those belonging to the first layer, and so on. Clearly, the "impact" takes some finite amount of time, however small. However, at present, we have no knowledge of the duration of the impact. Therefore, of necessity, we have to assume that the impact is instantaneous. As we shall see, in spite of this assumption, the comparison between theory and experiment is quite reasonable. The mechanisms of energy dissipation are inelastic collisions and frictional sliding amongst the particles, and between the particles and the enclosure walls. Since we cannot estimate the amount of energy dissipated by each of these mechanisms, we "wrap"

all of the mechanisms of energy dissipation into an "effective coefficient of restitution", $R$. Consider a collinear impact between $m$ and $M_2$. Let $v$ be defined as the velocity in the positive $z$ direction. Let $v_p^-$ ($v_p^+$) and $v_2^-$ ($v_2^+$) be the velocities of the particle and the primary mass before(after) the impact. Then $R$ is defined as

$$R = -\frac{(v_p^+ - v_2^+)}{(v_p^- - v_2^-)}, \quad 0 \leqslant R \leqslant 1. \tag{7}$$

Applying the conservation of linear momentum, the velocities after the impact are given by

$$v_2^+ = \frac{(1 - R\mu)\, v_2^- + \mu(1 + R) v_p^-}{(1 + \mu)} \quad \text{and} \quad v_p^+ = \frac{(1 + R)\, v_2^- + (\mu - R) v_p^-}{(1 + \mu)}, \tag{8a, b}$$

where the mass ratio is defined as $\mu = m/M_2$. Invoking the conservation of energy, the kinetic energy converted into heat during the impact may be shown to be

$$\Delta T = \frac{1}{2}(1 - R^2)\frac{m}{1 + \mu}(v_p^- - v_2^-)^2. \tag{9}$$

We shall estimate $R$ by minimizing the difference between theory and experiment using the Gauss' method of least squares.

In the following, we describe a simple methodology by which the motion of the particles and the primary mass can be tracked for all $t > 0$. Figure 13 contains time domain representations of the motion of the particle and the primary mass for a representative value of $R = 0{\cdot}4$ and various initial amplitudes. Reference will be made to this figure throughout this work. At time $t = 0$, let the particles be in contact with the primary mass (Case 1). Let $M_1$ be released from rest (i.e., the initial velocity, $v_0 = 0$) with an initial displacement, $u_0 = -U_0$. The motion of the primary mass and particles is described by equation (5). The particles remain in contact with the *floor* of the enclosure until the acceleration of $M_1$ along the negative $z$ direction exceeds the acceleration due to gravity, i.e., separation occurs when

$$(-a) > g. \tag{10}$$

For later use, it is noted that if the particles had been moving in contact with the *ceiling* of the enclosure, the separation would have occurred when

$$(-a) < g. \tag{11}$$

Together, equations (10) and (11) will be called the *separation criterion*. Throughout this work we will use equations (5) and (equations (10) or (11)) for calculating the moment of separation. However, it is interesting as well as instructive to note that *for a perfectly elastic beam* ($\psi_b = 0$), equation (5) and equation (10) or (11) lead to a simple expression for the displacement at which separation occurs, namely, $u_s \equiv g/\omega_1^2$. As an example, at 20 Hz, $u_s = O(1\text{ mm})$; at 1 kHz, $u_s = O(0{\cdot}1\ \mu\text{m})$. (When the intrinsic damping in the beam is small, as is the case in our experiments, the exact $u_s$ was found to be very close to $g/\omega_1^2$.) Moreover, if $g = 0$ (for space applications) or for motion in the horizontal plane, $u_s = 0$ regardless of $\psi_b$. Let $v_s$ be the "launch velocity" of the particles at the time of separation, $t_s$. After separation, the particles "free fall" under the influence of gravity, and their motion is given by

$$u_p(t) = u_s + v_s(t - t_s) - \tfrac{1}{2} g(t - t_s)^2, \quad t_s < t < t_1, \tag{12}$$

where $t_1$ is the instant at which the particles suffer their first impact. After separation, the motion of $M_2$ is given by equation (6). There are two different scenarios for the first impact to occur: (1) if the clearance, $d$, is sufficiently small such that the "ceiling impact criterion", $u_p = u_2 + d$, is satisfied, then the first impact of the particle will be with the ceiling; otherwise (2) the first impact will occur with the floor when the "floor impact criterion", $u_p = u_2$, is satisfied. The transition occurs when the particle makes an osculating contact with the ceiling, i.e., when the displacement trajectories of the particle and the ceiling have a common tangent at the point of contact. This is shown graphically in Figure 13(b).

We now consider the motion after the first impact. At the risk of stating the obvious, for any $R \neq 0$, the particles will continue to bounce ad infinitum. In order to limit the number of impacts to some reasonable value without introducing an appreciable error in computing $\Psi$, we introduce the following approximation. Subsequent to an impact, let $\varepsilon$ be the ratio of the speed of the particle relative to the primary mass to the speed of the primary mass, i.e., $\varepsilon = (v_p^+ - v_2^+)/v_2^+$. Let $\delta = \frac{1}{2}m((v_p^+)^2 - (v_2^+)^2)/\frac{1}{2}M_1(v_2^+)^2$; $\delta$ is a dimensionless measure of the kinetic energy of the particles that is ignored during this approximation. As $\varepsilon \to 0$, $\delta \to 0$, but the number of impacts becomes intractably large. By trial and error it was found that $\varepsilon = 0{\cdot}05$ resulted in a reasonable compromise between the number of impacts and the error in computing $\Psi$. When $\varepsilon = 0{\cdot}05$, $\delta$ is merely 0·01, which can be safely neglected. Therefore, for $\varepsilon > 0{\cdot}05$, the motion after an impact is calculated by equations (6) and (12). When $\varepsilon \leqslant 0{\cdot}05$, then $v_p^+$ is set equal to $v_2^+$, i.e., in the analysis the particles are not allowed to have any more rebounds. The subsequent motion of the primary mass plus the particles ($M_1$) is calculated by using equation (5). The separation criterion (equation (10) or (11)) is used to fix the moment of the next separation, and the process continues.

Traditionally, the specific damping capacity is defined as $\Psi = \Delta W/W$, where $\Delta W$ is the stored elastic energy converted into heat during one cycle, and $W$ is the maximum stored elastic energy during the cycle. It is customary to view $W$ as a function of strain tensor (hence the expression "strain energy density" for $W$). In the context of particle impact damping, it is more appropriate to define specific damping capacity as

$$\Psi = \Delta T/T, \tag{13}$$

where $\Delta T$ is the kinetic energy converted into heat during one cycle, and $T$ is the maximum kinetic energy during the cycle. With reference to Figure 13(a), we define a cycle to be the duration between two successive maxima, $V$, of the primary mass *velocity curve*, $v(t)$, rather than the displacement or the acceleration curves. Then, $T$ is maximum at the start of a cycle and is given by

$$T = \tfrac{1}{2}M_1V^2. \tag{14}$$

Next, we calculate the energy dissipated during the $i$th cycle, $\Delta T_i = T_i - T_{i+1}$. If the particles are in contact with the enclosure at *both* velocity peaks, then

$$\Delta T_i = \tfrac{1}{2}M_1(V_i^2 - V_{i+1}^2). \tag{15}$$

Substituting equations (14) and (15) into equation (13),

$$\Psi_i = \frac{V_i^2 - V_{i+1}^2}{V_i^2}. \tag{16}$$

When the particles are not in contact with the enclosure at either of the velocity peaks, equations (15) and (16) are no longer valid. Then, the energy dissipated during a cycle must

be computed by summing the energy dissipated due to all of the impacts ($N$) during the cycle by the use of equation (9), i.e.,

$$\Delta T_i = \sum_{n=1}^{N} \Delta T^{(n)}. \tag{17}$$

Once again $\Psi_i$ is computed by substituting equations (14) and (17) into equation (13). Since, as we shall see in Figure 6, particle impact damping is highly non-linear, $\Psi_i$ must be determined for each cycle. The traditional methods—where damping is measured by averaging over a large number of cycles—would greatly reduce the usefulness of the data so obtained.

### 2.3. DIMENSIONAL ANALYSIS

A dimensional analysis using the Buckingham pi theorem was carried out to reveal the appropriate dimensionless parameters. The energy dissipated per cycle by the particles, $\Delta T$, is written as

$$\Delta T = f_1(m, d, g, M_1, \omega_1, U; R). \tag{18}$$

The physical quantities $M_1$, $\omega_1$, and $U$ are chosen to reduce the number of independent variables from eight to five:

$$\Psi = f_2(\mu, \alpha^{-1}, \Gamma^{-1}; R), \tag{19}$$

where $\Psi = \Delta T/\frac{1}{2}M_1(\omega_1 U)^2$ = dimensionless energy dissipated per cycle, $\mu = m/(M_1 - m) = m/M_2$ = mass ratio, $\alpha = U/d$ = dimensionless displacement amplitude, and $\Gamma = U\omega_1^2/g$ = dimensionless acceleration amplitude, in units of $g$.

The semicolon separating $R$ is used to emphasis that $R$ is obtained by "curve-fitting" the experimental data to the model. When we present experimental results, we will find extensive use for the dimensionless clearance

$$\Delta \equiv \frac{d\omega_1^2}{g} = \frac{\Gamma}{\alpha}. \tag{20}$$

For PID in a gravitational field we will view

$$\Psi = f(\mu, \Delta, \Gamma; R). \tag{21}$$

On the other hand, in situations where $g$ drops out of equation (18)—in a zero-gravity environment, when $g \ll U\omega_1^2$, or for motion in the horizontal plane—equation (19) reduces to

$$\Psi = f(\mu, \alpha; R). \tag{22}$$

Finally, for presenting the time domain data we introduce a dimensionless time as $\tau = \omega_1 t$.

## 3. EXPERIMENTAL PROCEDURES

A schematic of the test set-up is shown in Figure 2. Both the enclosure and the beam are made up of 3003 aluminum alloy (Young's modulus, $E = 70$ GPa and density $= 2{\cdot}7$ g/cm$^3$).

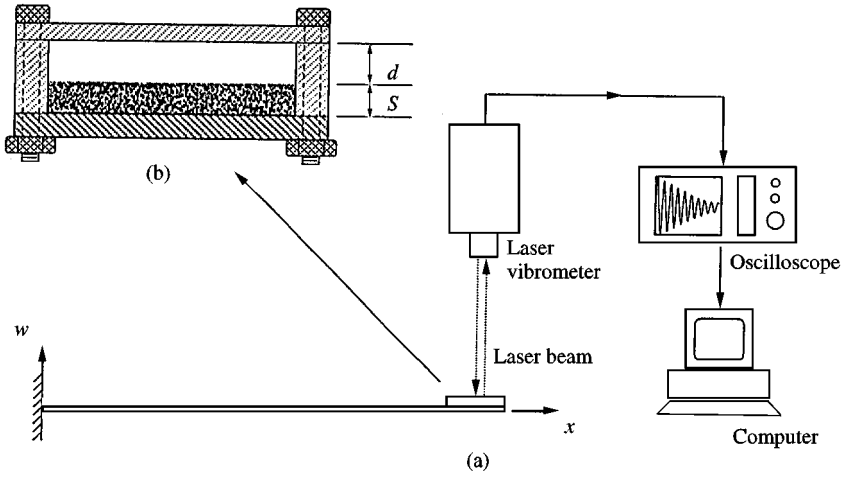


Figure 2. (a) A schematic of the experimental arrangement. (b) A magnified view of the particles inside the enclosure (drawn to scale).

The beam dimensions are: length, $L = 25{\cdot}4$ cm, width $= 3{\cdot}18$ cm, and height $= 0{\cdot}23$ cm. The mass of the enclosure is 19·4 gs, and its interior dimensions are: diameter $= 2{\cdot}54$ cm, and height $= 0{\cdot}254$ cm, 0·508 cm, or 0·762 cm. The particle bed depth, $s$, serves only to define the total mass of the particles, $m = \rho As$, where $\rho$ is the mass per unit volume occupied by the particles and $A$ is the cross sectional area of the interior of the enclosure. The clearance, $d$, is the distance between the top of the bed of particles at rest and the ceiling of the enclosure.

At time $t = 0$, the beam is given a tip displacement, $U_0$, released from rest, and allowed to decay freely; the beam vibrates in its fundamental mode. An OFV300 Polytec laser vibrometer is used to measure the *velocity* of the enclosure. A piece of lightweight retroreflecting tape is attached to the top center of the enclosure for reflecting the incident laser beam. Using the well-known Doppler effect and the principle of heterodyne interferometry, the velocity is measured by frequency demodulation to an extremely high resolution of 1 μm/s. In our experiments, the velocity amplitude ranges from 30 to 2000 mm/s. Consequently, the minimum ratio of the measured velocity amplitude to the velocity resolution ("signal-to-noise ratio") is $3 \times 10^4$. Data acquisition is triggered at $t = 0$, and the decaying waveform is collected with a Yokogawa DL708 Digital Processing Oscilloscope (DPO). The DPO has a 16-bit vertical resolution (1 part per 65 536), a maximum digitizing rate of $10^5$ points/s (i.e., a 10 μs interval) and a maximum record length of $4 \times 10^6$ points. We use a digitizing rate of 2000 points/s. For a nominal frequency of 18 Hz observed in this study, this translates to 111 points/cycle.

Lead powder was the material used in this study. The powder consisted of irregularly shaped particles (commercially known as "lead dust") whose average size was 230 μm. The total mass of particles was kept constant at 4·0 g throughout this experimental investigation. Thus, the mass ratio, $\mu = 0{\cdot}12$, was kept constant. Three different clearances were investigated: $d = 1{\cdot}27$, 3·81 and 6·35 mm (or $\Delta_1 = 1{\cdot}62$, $\Delta_2 = 4{\cdot}87$, and $\Delta_3 = 8{\cdot}11$, respectively). For each clearance, the test was repeated with 18 different initial amplitudes in the range $1 < \Gamma < 25$. For each test the frequency, $\omega$, was determined from the time interval between successive zero crossings averaged over all of the cycles in that test. Without the particles the calculated frequency is $\omega_2 = 18{\cdot}86$ Hz. The average of eight measurements is $\omega_2 = 18{\cdot}61$ Hz, and the standard deviation is 0·07 Hz. With particles the calculated

frequency is $\omega_1 = 17{\cdot}82$ Hz; the measured frequency is $\omega_1 = 17{\cdot}77$ Hz, and the standard deviation is 0·15 Hz. Energy dissipated per cycle, $\Delta T_i$, and damping, $\Psi_i$, were determined for *each cycle* using equations (15) and (16) respectively.

## 4. EXPERIMENTAL RESULTS

A comparison of typical experimental waveforms with and without lead powder is shown in Figure 3. A dramatic increase in the attenuation due to the presence of particles is clearly evident. The kinetic energy dissipated per cycle with and without particles, derived from Figure 3 using equation (15), is presented in Figure 4 as a function of $V$, the velocity at the beginning of each cycle. The corresponding damping, calculated using equation (16) is shown in Figure 5 as a function of dimensionless acceleration amplitude, $\Gamma = V\omega/g = U\omega^2/g$. For completeness, the root strain or the strain amplitude at the base of the cantilevered beam is also shown. It is interesting to note that in Figure 4, for the case of the beam with particles, $\Delta T$ continues to increase monotonically with $V$, while the corresponding damping in Figure 5 rises dramatically to a peak and then decreases gradually. This is merely a consequence of the fact that the kinetic energy (denominator in equation (13)) is proportional to the *square* of the velocity. (As a minor but interesting aside, we calculate the increase in temperature of the lead particles during one cycle under the assumption that all of the energy converted into heat is absorbed by the lead particles: 10 mJ absorbed by 4 g of lead corresponds to an increase in temperature of merely 0·02 K.)

Because these results are a compilation of 18 individual tests each with a different starting point, the path of the individual tests shown in Figures 4 and 5 is traced by thin solid lines. A striking observation is that at a particular value of $\Gamma$, $\Psi$ depends (albeit slightly) on whether that point is the first cycle of a test that was started at $\Gamma$, or (say) the fifth cycle of

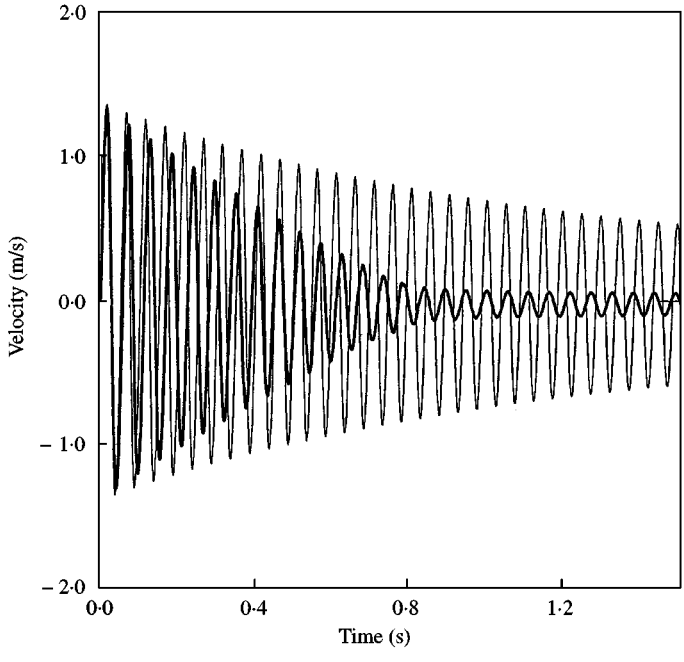


Figure 3. A comparison of typical experimental velocity waveforms: ——, without particles; ——, with particles ($d = 3{\cdot}81$ mm).

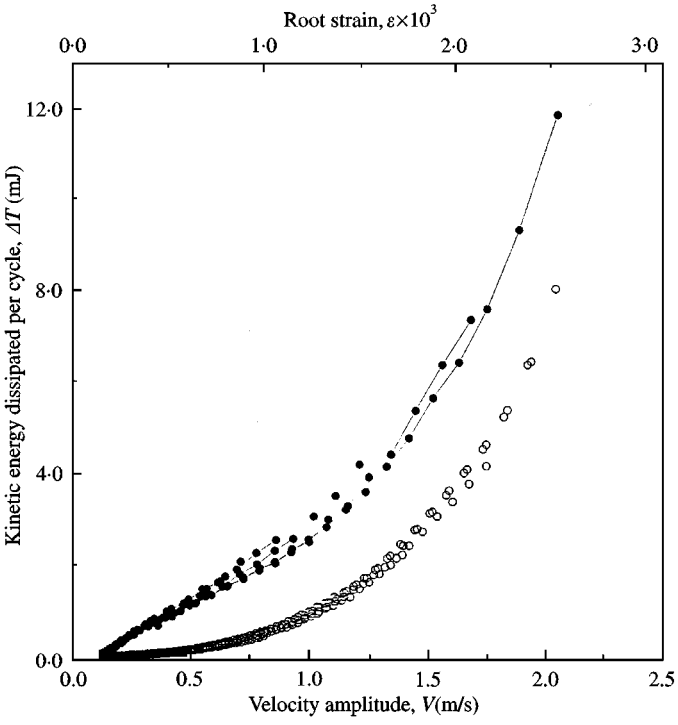


Figure 4. Kinetic energy dissipated per cycle versus velocity amplitude: ○, without particles; —●—, with particles ($d = 3{\cdot}81$ mm).

a test that was started at a higher value of $\Gamma$: $\Psi$ *is not a single-valued function of* $\Gamma$. Since the variations in $\Psi$ are rather small, we will use the following approach to make $\Psi$ a single-valued function of $\Gamma$. In the analysis, $\Psi$ will be calculated only for the first cycle of a "simulated test" (the rest of the motion will be ignored) and assigned to the value of $\Gamma$ at the start of the "simulated test". The calculated $\Psi$ will be compared with the $\Psi$ measured at that value of $\Gamma$; the latter could correspond to any cycle of the (actual) test. The reasons for this decision will be discussed in some detail later in the paper.

In the absence of particles, the measured damping is due to the intrinsic material damping of the aluminum beam, $\psi_b$. In Figure 5, the best-fit straight line through these data are shown as a thick solid line. The damping due to particles alone (PID) is determined by subtracting $\psi_b$ from the total damping with particles. For the same mass ratio, $\mu = 0{\cdot}12$, the particle impact damping, $\Psi$, is shown in Figure 6 for three values of dimensionless clearance, namely, $\Delta_1 = 1{\cdot}62$, $\Delta_2 = 4{\cdot}87$, and $\Delta_3 = 8{\cdot}11$. The damping in the *first cycle* of each test is marked by the corresponding filled symbols. The maximum damping is $\Psi_{max} = 0{\cdot}5$. This is more than an order of magnitude greater than the intrinsic material damping of most structural metals (aluminum, steel, brass, etc.) which is $O(1\%)$.

From equation (10) it follows that if $(-a) < g$, i.e., $\Gamma \leqslant 1$, the particles always remain in contact with the floor, i.e., the calculated PID is zero for any choice of $\mu$, $\Delta$ or $R$. With this in mind we re-examine Figure 6. As $\Gamma \to 1^+$, $\Psi$ decreases very rapidly. In the range, $0 < \Gamma < 1$, $\Psi$ is very small. However, $\Psi$ is not exactly equal to zero. We offer a plausible conjecture for this observation. In the data presented in Figure 6, all but one test were started at some value of $\Gamma > 1$. Even when $\Gamma$ falls below one, the particles may still be "bouncing around" in the enclosure leading to a small but non-zero $\Psi$ for $\Gamma \leqslant 1$. To test this conjecture, one test

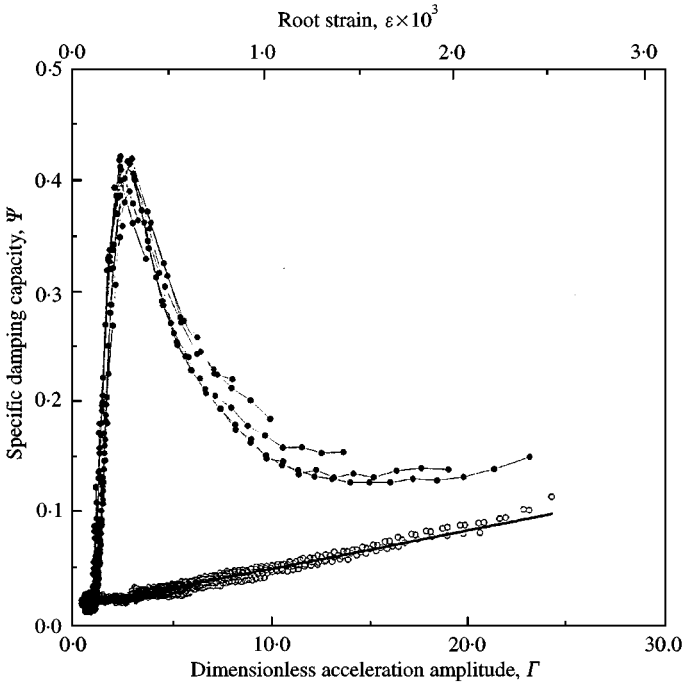


Figure 5. Specific damping capacity of the system versus dimensionless acceleration amplitude: ○, without particles; —●—, with particles; ——, the least-squares-fit straight line, $\psi_b = 0{\cdot}0035\Gamma + 0{\cdot}015$. ($d = 3{\cdot}81$ mm.)

was especially conducted where the starting $\Gamma$ was chosen to be slightly less than unity. The results are presented at the top of Figure 6 on a highly magnified scale: $\Psi = O(0{\cdot}1\%)$ which is comparable to the measurement errors. This supports our conjecture.

## 5. NUMERICAL RESULTS AND COMPARISON WITH EXPERIMENT

### 5.1. PID IN THE ABSENCE OF THE CEILING

#### 5.1.1. *Numerical results*

A striking feature of the data in Figure 6 is that in the range $0 < \Gamma < 1{\cdot}75$, $\Psi$ is measurably identical for $\Delta_1$, $\Delta_2$, and $\Delta_3$, and that in the range $0 < \Gamma < 2{\cdot}5$, $\Psi$ is identical for $\Delta_2$ and $\Delta_3$. Moreover, at $\Gamma = 1{\cdot}75$, $2{\cdot}5$, and $3{\cdot}5$ respectively, $\Psi(\Gamma, \Delta_1)$, $\Psi(\Gamma, \Delta_2)$, and $\Psi(\Gamma, \Delta_3)$ reaches a maximum. In the following, we will show that these maxima occur when the particles impact the ceiling.

For a fixed clearance $\Delta$ (or $d$, since $\omega_1$ and $g$ are fixed in the present work), $\Gamma$ (or $U$) can always be chosen sufficiently large such that upon leaving the floor, the first impact of the particles occurs with the ceiling. Similarly, $\Gamma$ can always be chosen sufficiently small such that the particles reach their apogee before impacting the ceiling and—accelerated by gravity—stay abreast of the ceiling during their downward journey. Under these circumstances, the first impact occurs with the floor; this is illustrated in Figure 13(a). The two regimes of $\Gamma$ are separated by a value of $\Gamma$ for which the particles suffer an osculating contact with the ceiling, i.e.,

$$u_p = u_2 + d \quad \text{and} \quad \mathrm{d}u_p/\mathrm{d}t = \mathrm{d}u_2/\mathrm{d}t. \tag{23}$$

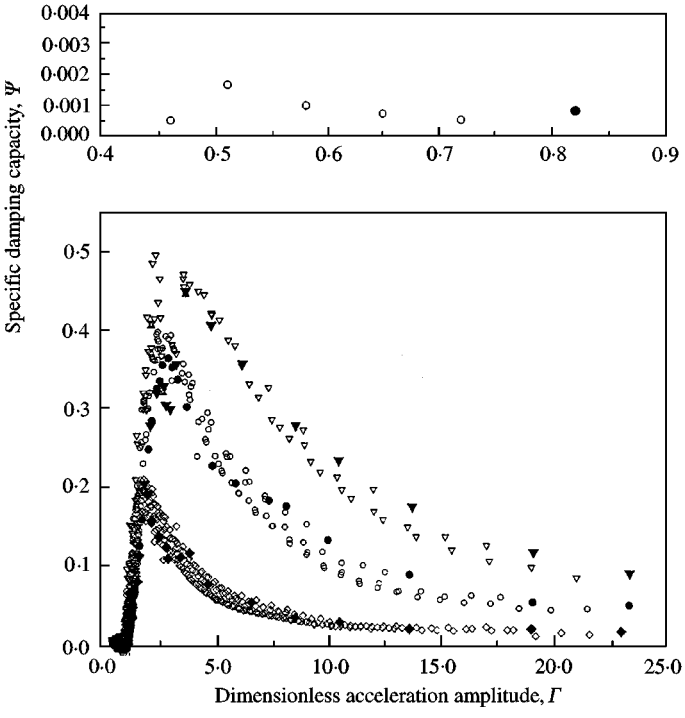


Figure 6. Specific damping capacity, due to particles only, for three clearances. All cycles: ◇, $\Delta_1 = 1{\cdot}62$; ○, $\Delta_2 = 4{\cdot}87$; ▽, $\Delta_3 = 8{\cdot}11$. The first cycle of each test is indicated by a filled symbol.

This is illustrated in Figure 7(a), and we will call it the osculation condition. Evidently, this critical value of $\Gamma$ depends upon $\Delta$, i.e., $\Gamma = f(\Delta)$ or $\Delta = f(\Gamma)$; we shall refer to this pair as $(\Delta^{cr}, \Gamma^{cr})$. Let $\bar{\tau} = \tau - \tau_s$ be the time measured from the moment of separation; recall that $\tau = \omega_1 t$. Let $\eta = \omega_1/\omega_2$, $\lambda = mg/K_2$, and $q = (\Gamma^2 - 1)^{1/2}$. Then $\mathrm{d}u_p/\mathrm{d}t = \mathrm{d}u_2/\mathrm{d}t$ leads to the transcendental equation

$$\frac{v_s}{\omega_2 U}\cos(\bar{\tau}) + \left[\frac{\lambda}{U} - \frac{u_s}{U} - \zeta\frac{v_s}{\omega_2 U}\right]\sin(\bar{\tau}) = \mathrm{e}^{\zeta\bar{\tau}}\left(\frac{v_s}{\omega_2 U} - \frac{\eta^2\bar{\tau}}{\Gamma}\right). \tag{24}$$

For an elastic beam, equation (24) reduces to

$$\eta q\cos(\bar{\tau}) + \left(\frac{\lambda\Gamma}{U} - 1\right)\sin(\bar{\tau}) = \eta(q - \eta\bar{\tau}). \tag{25}$$

For a fixed $\Gamma$, equation (24) fixes the time of osculation. Next, the condition $u_p = u_2 + d$ leads to the following equation for $\Delta$:

$$\Delta = \frac{u_s\Gamma}{U} + \frac{v_s\Gamma}{\omega_2 U}\bar{\tau} - \frac{1}{2}(\eta\bar{\tau})^2 - \frac{\lambda\Gamma}{U} - \Gamma e^{-\zeta\bar{\tau}}\left[\left(\frac{u_s}{U} - \frac{\lambda}{U}\right)\cos(\bar{\tau}) + \left(\frac{v_s}{\omega_2 U} + \zeta\left(\frac{u_s}{U} - \frac{\lambda}{U}\right)\right)\sin(\bar{\tau})\right]. \tag{26}$$

For an elastic beam this reduces to

$$\Delta = 1 + \eta q\bar{\tau} - \frac{1}{2}(\eta\bar{\tau})^2 - \frac{\lambda\Gamma}{U} - \left(1 - \frac{\lambda\Gamma}{U}\right)\cos(\bar{\tau}) - \eta q\sin(\bar{\tau}). \tag{27}$$

For the particular $\zeta$ measured in this work, the solution of equations (24) and (26) is plotted in Figure 7(b). The three particular values of $\Delta$ used in this work are indicated by filled circles. For a fixed $\Delta$, if $\Gamma < \Gamma^{cr}$, the particles are oblivious of the ceiling and, therefore, $\Psi$ is independent of $\Delta$. With this, we return to Figure 6. It now becomes obvious why $\Psi$ is the same for $\Delta_1$, $\Delta_2$, and $\Delta_3$ for $0 < \Gamma < 1{\cdot}75$, and $\Psi$ is the same for $\Delta_2$ and $\Delta_3$ for $0 < \Gamma < 2{\cdot}5$. Moreover, $d$ drops out of equation (18), and equation (19) reduces to

$$\Psi = f_3(\mu, \Gamma; R). \tag{28}$$

For completeness, the fact that $\Psi = 0$ when $\Gamma < 1$ is shown as the shaded area. Finally, when $\Gamma < \Gamma^{cr}$, we can remove the ceiling with impunity. The subscript $(\ )_0$ will be used to denote all results obtained in the absence of a ceiling. The subscripts $(\ )_1$, $(\ )_2$, and $(\ )_3$, will be used to denote results corresponding to $\Delta_1$, $\Delta_2$, and $\Delta_3$, respectively.

We begin by analyzing the damping due only to the first impact with the floor; this will be denoted by $\Psi_0^{FID}$. A kinematic analysis is presented first. For several discrete values of $\Gamma$ the normalized displacement and velocity of the primary mass and the particles are plotted in Figure 8. The particle trajectories are terminated at the instant of the first impact. When $\Gamma = 2{\cdot}86$, the primary mass executes one full cycle prior to the impact. For $\Gamma > 2{\cdot}86$, the first impact occurs during the second cycle. For later use, this particular value of $\Gamma$ will be denoted by $\Gamma_0^{(2)}$; then, $\Gamma_0^{(2)} = 2{\cdot}86$. Similarly, when $\Gamma > 5{\cdot}94$, the first impact occurs during the third cycle, and $\Gamma_0^{(3)} = 5{\cdot}94$, and so on.

For no particular reason, taking $R = 0$ (i.e., a completely plastic impact with no rebound), $\Psi_0^{FID}$ calculated by using equations (9) and (13) is plotted in Figure 9. The first impact

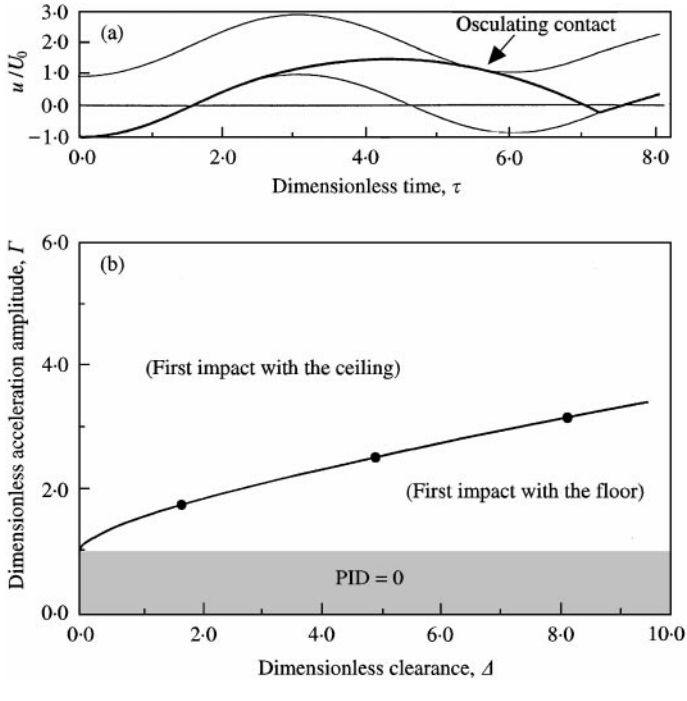


Figure 7. (a) Normalized displacement of the primary mass (——) and of the particles (——). $\Gamma = \Gamma_2^{cr} = 2{\cdot}55$, $\Delta = \Delta_2 = 4{\cdot}87$, $R = 0$. (b) A graph of the osculation condition. The three particular clearances used in the experiments are indicated by filled circles.

damping (FID) for any other value of $R$ is given in terms of FID for $R = 0$ by

$$\Psi_0^{FID}(R) = (1 - R^2)\Psi_0^{FID}(0). \tag{29}$$

The velocities just before the impact, $v_p^-$ and $v_2^-$, are also shown. With references to equations (9) and (13), $\Psi_0^{FID}$ is proportional to $(v_r^-)^2$, where the normalized impact velocity, $v_r^- = (v_p^- - v_2^-)/\omega_1 U_0$. For convenience of the reader, in Figure 8, for one value of $\Gamma = 2$ $v_p^-$ and $v_2^-$ are connected by a dark vertical line whose length equals $v_r^-$. As expected, as $\Gamma$ increases from unity, $\Psi_0^{FID} \to 0$ increases. However, an extremely counter-intuitive observation is that as $\Gamma \to 4{\cdot}38$, $\Psi_0^{FID} \to 0$. The reasons become immediately clear when we examine the velocity curves: at $\Gamma = 4{\cdot}38$, there is an "osculating impact" ($v_r^- = 0$). The launched particle is recaptured by the beam with no loss of energy. (This situation is reminiscent of how a good cricket player catches a fast-moving ball with his bare hands.) At $\Gamma = 2{\cdot}49$, $\Psi$ reaches its first maximum; this is denoted by $\Psi_0^{FIDmax1}$. Here, $v_p^-/\omega_1 U_0$ and $v_2^-/\omega_1 U_0$ are (roughly) equal and opposite, and their magnitudes are (roughly) equal to unity. (This is reminiscent of a head-on collision of two identical cars moving with equal speeds, which, as we know, causes maximum damage.) If we set $v_p^-/\omega_1 U_0 = v_2^-/\omega_1 U_0 = 1$

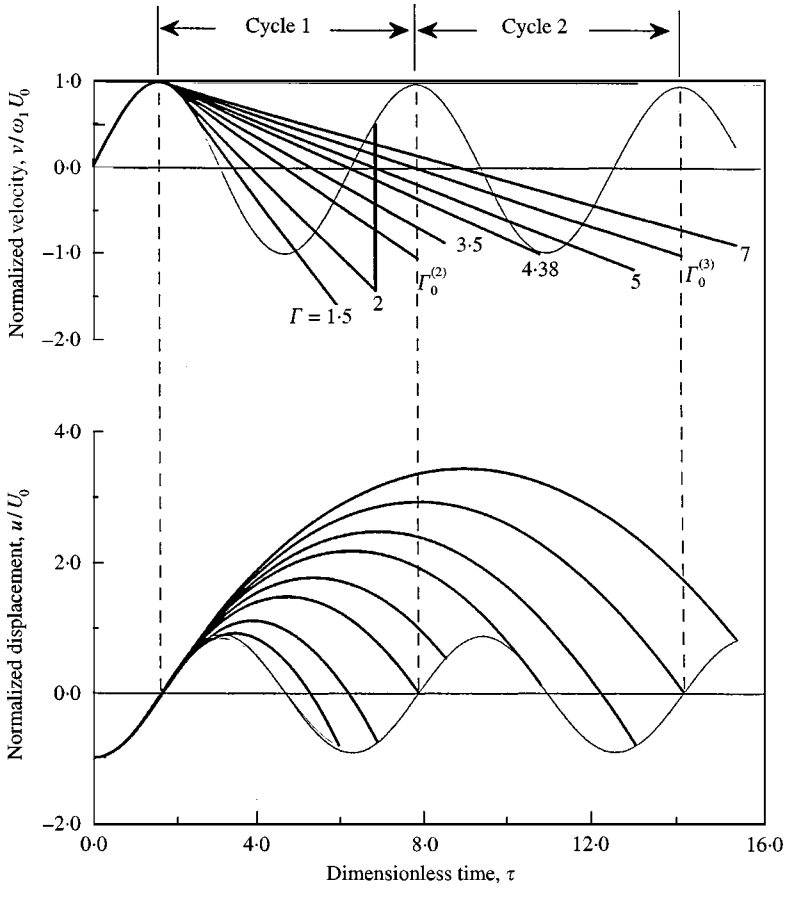


Figure 8. Normalized displacement and velocity of the primary mass (——) and of the particles (——) for various initial amplitudes up to the first impact. No ceiling.

(exactly), from equations (9) and (13) we obtain a *closed-form expression*

$$\Psi_0^{FIDmax} = 4(1 - R^2)\frac{\mu}{(1+\mu)^2}. \tag{30}$$

For a given $R$ and $\mu$, this is the maximum damping that can be obtained for an enclosure with no ceiling. As we shall see, this equation captures the functional dependence of $\Psi$ on $R$ and $\mu$.

Let the weight penalty be defined as

$$\beta = \frac{\text{mass of the particles}}{\text{mass of the cantilever beam}} = \frac{m}{M_b}. \tag{31}$$

Obviously, one would like to achieve a given $\Psi$ with a minimum $\beta$. By way of example, suppose we wish to achieve a maximum $\Psi = 50\%$. For a cantilevered beam without an end mass, the reduced mass, $M_2 = 0{\cdot}25M_b$, where $M_b = \gamma L$; therefore, $\mu = m/M_2 = 4m/M_b = 4\beta$. Taking $R = 0$, from equation (30), $\Psi_0^{FIDmax} \approx 50\%$ when $\mu = 20\%$, i.e., $\beta = 5\%$: A small weight penalty (5%) results in an order of magnitude larger maximum damping (50%). As a minor aside, when $R = 0$, $\Psi_0^{FIDmax} = 100\%$ (total cessation of all motion) can be achieved for $\mu = 1$, i.e., for a weight penalty of only 25%. In our experiments, for $\mu = 0{\cdot}12$ and $M_b = \gamma L + m_{encl}$, a maximum $\Psi = 50\%$ was achieved for

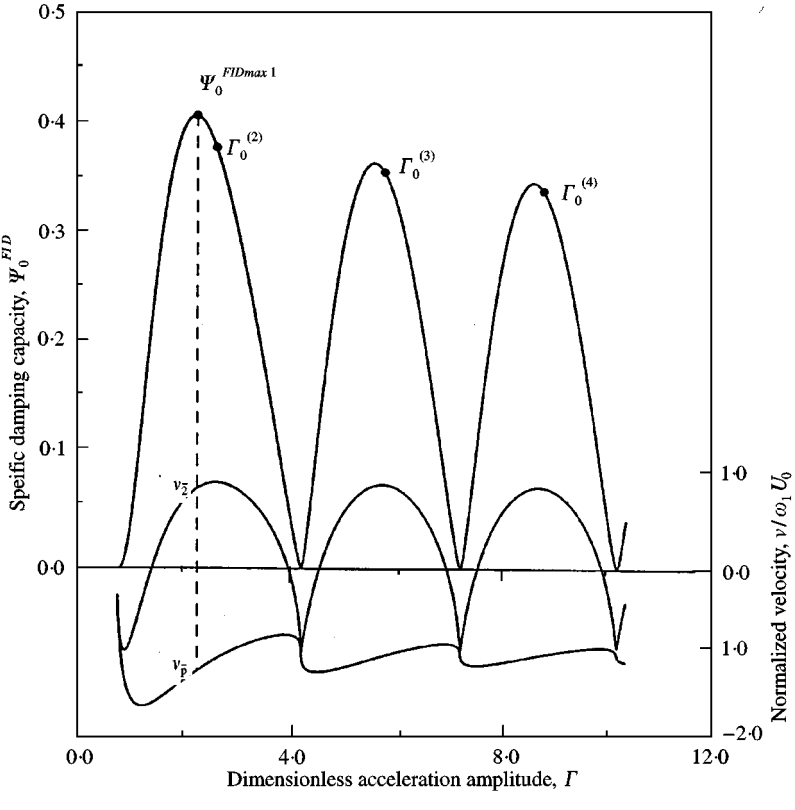


Figure 9. Specific damping capacity due to the first impact only $\Psi_0^{FID}$, and normalized velocity of the primary mass, $v_2^-$, and of the particles, $v_p^-$, just prior to the first impact. No ceiling. $R = 0$.

$\beta \approx 6\%$. (It will be shown that including a ceiling can result in a maximum $\Psi > \Psi^{F1Dmax}$.)

Next, we confine our attention to the range of $\Gamma$ where the first impact occurs during the first cycle, $1 < \Gamma \leqslant \Gamma_0^{(2)}$, and examine $\Psi_0$ in more detail. In the following calculations, a representative value of $R = 0{\cdot}4$ was used.

With reference to Figure 10(a), for a sufficiently small $\Gamma$, *all* impacts occur during the first cycle, i.e., the particles begin to move with the primary mass (or, the particles come to relative rest against the primary mass) before the end of the first cycle. For a representative value of $\Gamma = 1{\cdot}7$ in this range, the trajectories are shown in Figure 10(a); the total number of impacts, $N = 4$. Identical results for $\Psi_0$ are obtained by using either equations (16) or equations (13) and (17). As $\Gamma$ is gradually increased, a point comes where *the last impact* occurs in the second cycle; this happens when $\Gamma = \Gamma_0^A = 1{\cdot}74$. The results of these calculations are shown as the thickest line in Figure 11 (marked $R = 0{\cdot}4$).

In the range $\Gamma_0^A \leqslant \Gamma \leqslant \Gamma_0^{(2)}$, the first impact continues to occur in the first cycle, but at a minimum, the last impact occurs after the first cycle. For a representative value of $\Gamma = 1{\cdot}9$, the trajectories are shown in Figure 10(b). Since the particles are no longer in contact with the primary mass at the end of the first cycle, equation (16) cannot be used to calculate $\Psi_0$. Instead, $\Psi_0$ was calculated by the use of equations (13) and (17). At $\Gamma = \Gamma_0^B = 1{\cdot}94$, there is a visible jump discontinuity in $\Psi_0$; this may be explained as follows. Every time an impact crosses over from the first cycle to the second cycle, there is a jump discontinuity in $\Psi_0$. However, for $\Gamma < \Gamma_0^B$, these jumps are too small to be graphically visible. On the other hand, at $\Gamma = \Gamma_0^B$, we go from two impacts to only one impact during the first cycle. Therefore, the decrease in $\Psi_0$ is large enough to be visible.

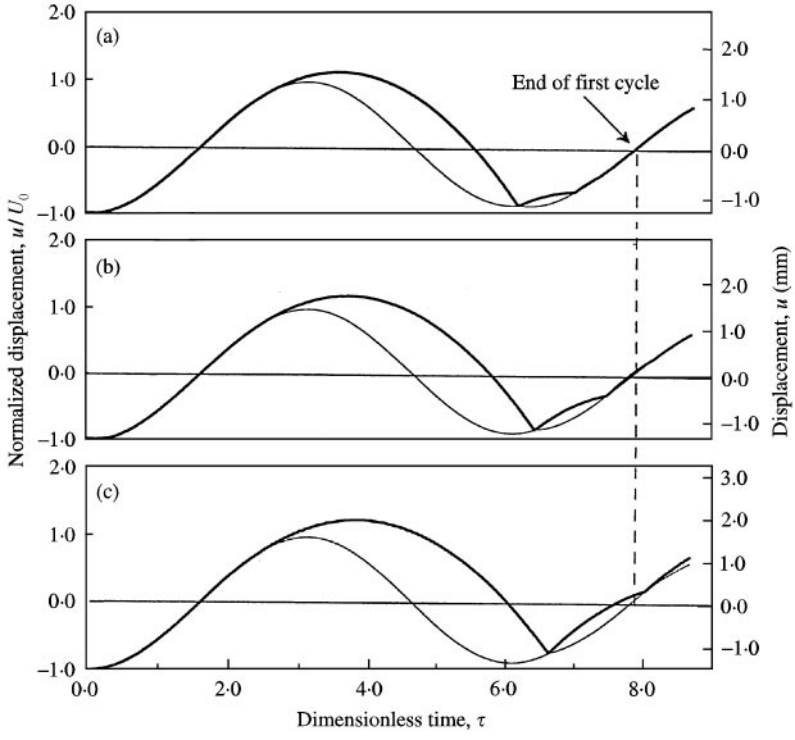


Figure 10. Displacement histories of the primary mass (——) and of the particles (——). No ceiling: $R = 0{\cdot}4$. (a) $\Gamma = 1{\cdot}7$, (b) $\Gamma = 1{\cdot}9$, (c) $\Gamma = 2{\cdot}0$.

For $\Gamma_0^B < \Gamma \leqslant \Gamma_0^{(2)}$, only the first impact occurs during the first cycle and, therefore, identically

$$\Psi_0 \equiv \Psi_0^{FID}, \quad \Gamma_0^B < \Gamma \leqslant \Gamma_0^{(2)}. \tag{32}$$

For comparison purposes, $\Psi_0^{FID}$ in the range $1 < \Gamma \leqslant \Gamma_0^{(2)}$ is reproduced from Figure 9 as a dashed line. The maximum damping occurs at $\Gamma \approx 2{\cdot}4$. (If the beam had been perfectly elastic, the maximum damping would have occurred at $\Gamma \approx 2{\cdot}5$.)

In order to study the sensitivity of $\Psi_0$ to $R$, in Figure 11 results are also plotted for $R = 0$, 0·2, 0·4, and 0·6. When $R = 0$, there is no rebound, and $\Psi_0$ and $\Psi_0^{FID}$ become identical. As $R$ increases, the characteristic points, $\Gamma_0^A$ and $\Gamma_0^B$, occur at successively lower values of $\Gamma$. In the range $1 < \Gamma < \Gamma_0^A$, all impacts occur in the first cycle and, therefore, $\Psi_0$ is independent of $R$. Substituting $\Psi_0$ for $\Psi_0^{FID}$ (0) in equation (29),

$$\Psi_0^{FID}(R) = (1 - R^2)\Psi_0, \quad 1 < \Gamma < \Gamma_0^A. \tag{33}$$

For comparison purposes, $\Psi_0^{FID}$ for $R = 0{\cdot}4$ is shown in the range $1 < \Gamma < \Gamma_0^B$ as the dashed line, and this proves to be a good approximation to $\Psi_0$. For $R = 0{\cdot}4$, using equation (33), the damping due to the first impact is 84% of the total damping.

Up to this point, for each initial amplitude, $\Gamma$, only the damping in the *first cycle* has been calculated. The first cycle damping, $\Psi_0$, as a function of initial amplitude, $\Gamma$, has been given in Figure 11. For each initial amplitude in the range $1 < \Gamma < \Gamma_0^A$, if the motion of the primary mass is followed past the first cycle, and $\Psi_0$ in the successive cycles is computed,

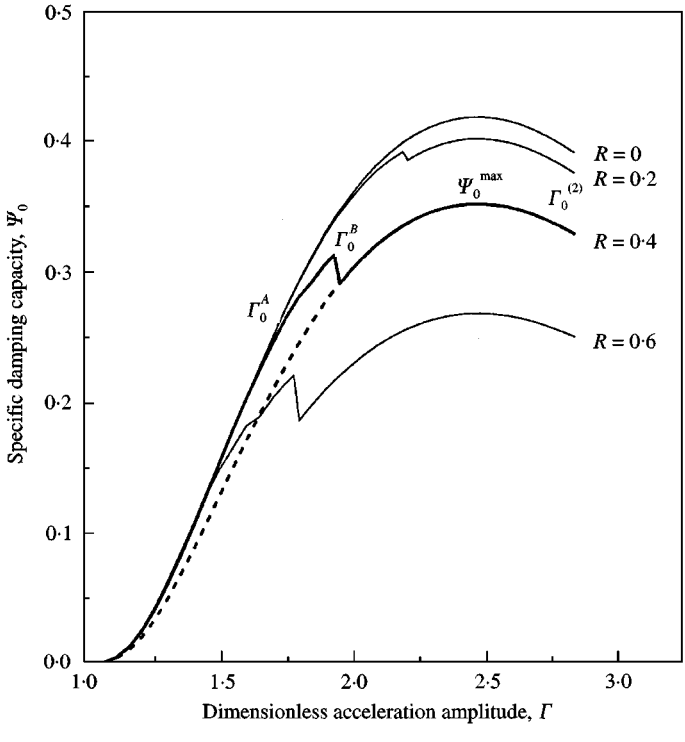


Figure 11. Damping for the case of no ceiling: ——, all impacts, $R = 0{\cdot}4$; ·····, first impact only ($\Psi_0^{FID}$), $R = 0{\cdot}4$; ——, influence of $R$ on $\Psi_0$.

then $\Psi_0$ will coincide with the first cycle damping curve. This occurs because the particles have come to relative rest with the primary mass at the end of each cycle before being launched in the next cycle. In the range $\Gamma_0^A \leqslant \Gamma \leqslant \Gamma_0^2$, the particles are not in contact with the primary mass at the end of the first cycle. For each initial amplitude, $\Gamma$, the damping in the subsequent cycles will be different than the first cycle damping curve until the amplitude falls below $\Gamma_0^A$, at which point the damping in subsequent cycles will equal first cycle damping. Consequently, significant scatter in the results is observed in the range $\Gamma_0^A \leqslant \Gamma \leqslant \Gamma_0^2$ because the damping in the subsequent cycles follows a different path for each initial $\Gamma$. To circumvent this problem, in the sequel, the theoretical $\Psi$ at any $\Gamma$ will mean the damping calculated during the first cycle of the motion starting with that $\Gamma$.

### 5.1.2. *Comparison between numerical results and experiment*

In Figure 6, *the measured first cycle damping* is indicated by filled symbols. In the range $0 < \Gamma < 4$, these data are reproduced in Figure 12. This particular range of $\Gamma$ was chosen to include all three $\Gamma^{cr}$, namely, $\Gamma_1^{cr} = 1{\cdot}75$, $\Gamma_2^{cr} = 2{\cdot}55$, and $\Gamma_3^{cr} = 3{\cdot}23$; these are indicated by dashed vertical lines. The prediction of the model using equations (13) and (17) (damping in the absence of the ceiling due to all impacts) is shown as the thick solid line covering the range $0 < \Gamma < \Gamma_0^2 = 2{\cdot}84$. (Recall that for $\Gamma > \Gamma_0^2$, the *first* impact occurs in the second cycle.) The model was curve-fitted to the combined data for all three $\Delta_j$ in the range $0 < \Gamma < \Gamma_j^{cr}, j = 1, 2, 3$; the best fit was obtained for $R = 0{\cdot}53$. In view of the simplicity of the model, the comparison between theory and experiments is considered remarkably good. Recall that at $\Gamma = \Gamma_j^{cr}$ the particles hit the ceiling. It is further reassuring to note that at $\Gamma_j^{cr}$ the theory and the experiment begin to deviate significantly. As a minor aside, the calculated first impact damping in the absence of the ceiling, $\Psi_0^{FID}$, for the same value of $R = 0{\cdot}53$ is plotted as a dashed line.

## 5.2. PID WHEN THE FIRST IMPACT OCCURS AT THE CEILING

### 5.2.1. *Numerical results*

Through a comparison of the theoretical $\Psi_0$ (no ceiling) and the experimental $\Psi$ (with ceiling) for $\Delta = \Delta_1$ in Figure 12, it is clear that the presence of the ceiling has a significant influence on $\Psi$. In this section, this influence is explored analytically. Using equations (13) and (17) and $R = 0{\cdot}4$, the damping is calculated as a function of $\Gamma$. For brevity, $\Psi(\Gamma, \Delta_1)$, $\Psi(\Gamma, \Delta_2)$, and $\Psi(\Gamma, \Delta_3)$ will be designated as $\Psi_1$, $\Psi_2$, and $\Psi_3$ respectively. These are shown in Figure 14 as the thickest solid lines. Intuitively, we had expected that accounting for an additional impact at the ceiling would always result in a higher damping: $\Psi_2$ and $\Psi_3$ do *increase*; $\Psi_1$, however, *decreases* rather sharply, and this may be explained as follows. The contribution to $\Psi_1$ of the impacts with the ceiling, $\Psi_1^C$, and of the floor, $\Psi_1^F$, is shown in Figure 14 as lines of medium thickness. For $\Gamma > \Gamma_1^{cr}$, clearly the rate of decrease of $\Psi_1^F$ is greater than the rate of increase of $\Psi_1^C$. The reason for the rapid decrease in $\Psi_1^F$ is that the impact with the ceiling significantly alters the *moment* of the second impact at the floor which, in turn, results in a significant decrease in the normalized impact velocity, and hence in $\Psi_1^F$. Time-domain representations of the impacts for $\Gamma = \Gamma_1^{cr} = 1{\cdot}75$ and for a slightly greater $\Gamma = 2{\cdot}3$, shown in Figures 13(b) and (c), respectively, illustrate this point. Turning our attention to $\Psi_2$ and $\Psi_3$, the effect of the first impact with the ceiling is to *increase* the total damping. Once again, the ceiling and floor contributions to the total damping were examined in detail for each of these cases. The rate of decrease of $\Psi^F$ was found to be smaller than the rate of increase of $\Psi^C$. Therefore, no general conclusions (i.e., conclusions that are

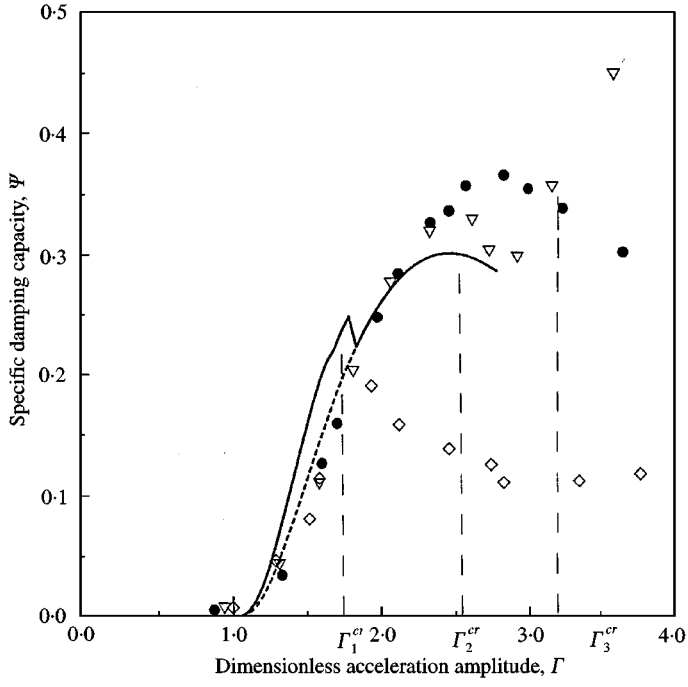


Figure 12. Comparison of theoretical damping with no ceiling to experimental results. ——, $\Psi_0$, equations (13) and (17); ·····, $\Psi_0^{FID}$, first impact only; ◇, $\Delta_1 = 1{\cdot}62$; ●, $\Delta_2 = 4{\cdot}87$; ▽, $\Delta_3 = 8{\cdot}11$. Best fit $R = 0{\cdot}53$.

independent of clearance, $\Delta$) can be drawn concerning the effect of the first impact with the ceiling on the total damping.

As $\Gamma$ increases, the number of impacts that occur with the floor and the ceiling also increase. With reference to Figure 14, the kinks in the curves correspond to those values of $\Gamma$ where an additional impact occurs. Turning our attention to the corresponding data in Figure 6, we note that these kinks are not observed in the experiments. We offer a plausible explanation for this observation. It is conjectured that in our experiments, the particles are traveling as a "cloud" rather than a single point mass as assumed in the model. Consequently, an impact between the particles and the floor (or the ceiling) occurs over some finite time period resulting in a smoothing of the kinks.

### 5.2.2. *Comparison between numerical results and experiment*

For the case of no ceiling, the experimental and theoretical results were compared in Figure 12. Now, we compare theoretical results (from Figure 14) with the *measured first cycle damping* in each test (from Figure 6) for $\Delta_j$, $\Gamma > \Gamma_j^{cr}$, $j = 1, 2, 3$; this is shown in Figure 15. The best fit for $\Psi_1$, $\Psi_2$, and $\Psi_3$ was obtained for $R = 0{\cdot}48$, $0{\cdot}48$, $0{\cdot}39$, respectively. We were pleasantly surprised to observe how well the theory captures the essential physics of PID for three substantially different clearances. Next, we examine in more detail the results in the vicinity of $\Gamma = \Gamma_j^{cr}$, $j = 1, 2, 3$, to determine how well the measurements capture the transition across $\Gamma_j^{cr}$. Experimental results for the first cycle damping in Figure 6 and theoretical results from Figures 12 and 15 are reproduced in Figure 16 in the range $0 < \Gamma < 5$. The experimental results very clearly capture the sudden changes in $\Psi$ at $\Gamma = \Gamma_j^{cr}$.

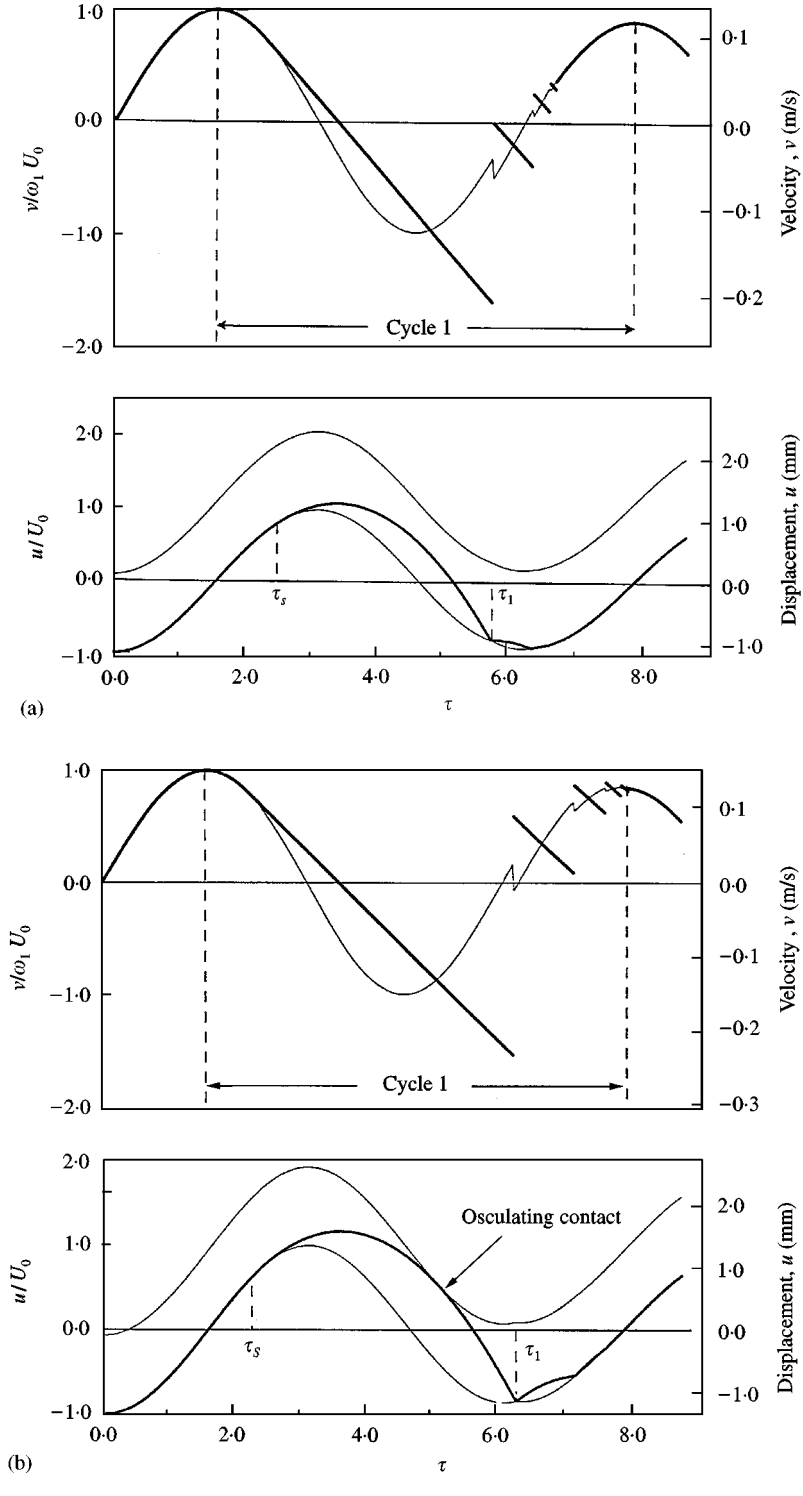


Figure 13. Displacement and velocity histories of the primary mass (——) and of the particles (——). $\Delta = 1{\cdot}62$, $R = 0{\cdot}4$. (a) $\Gamma = 1{\cdot}5$, (b) $\Gamma = \Gamma_1^{cr} = 1{\cdot}75$, (c) $\Gamma = 2{\cdot}3$, (d) $\Gamma = 12$.

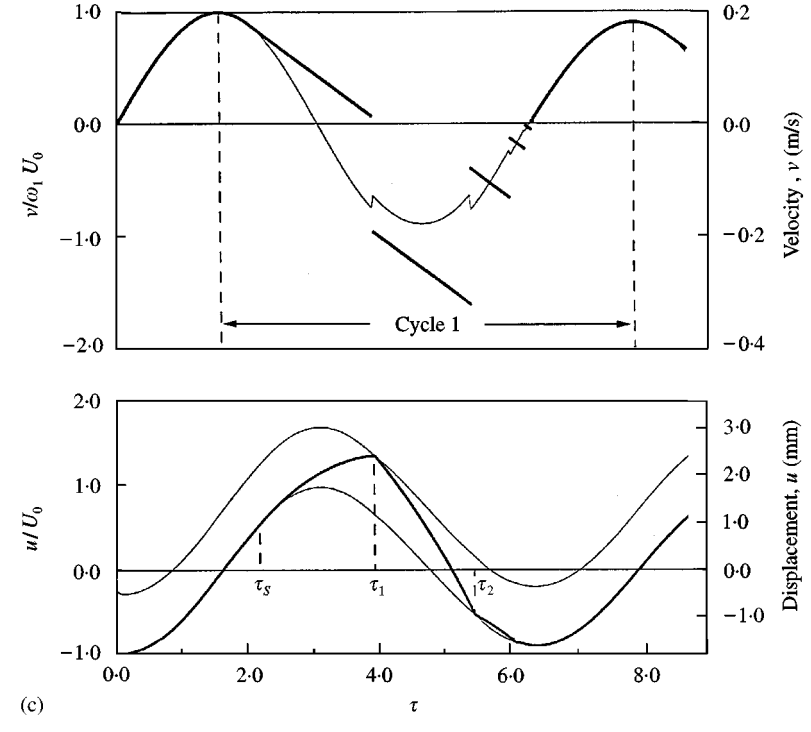


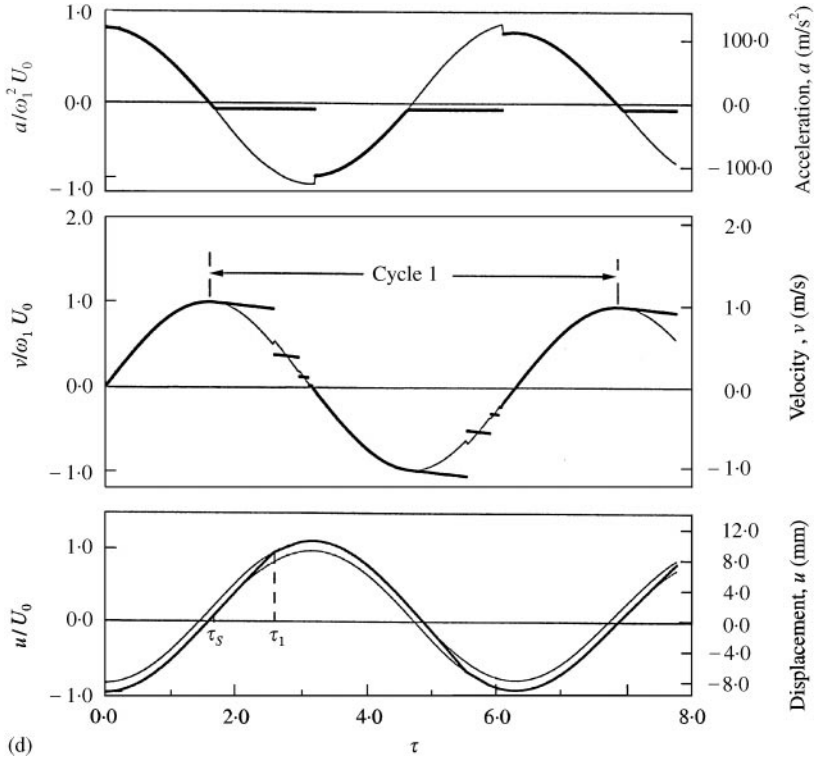


Figure 13. Continued.

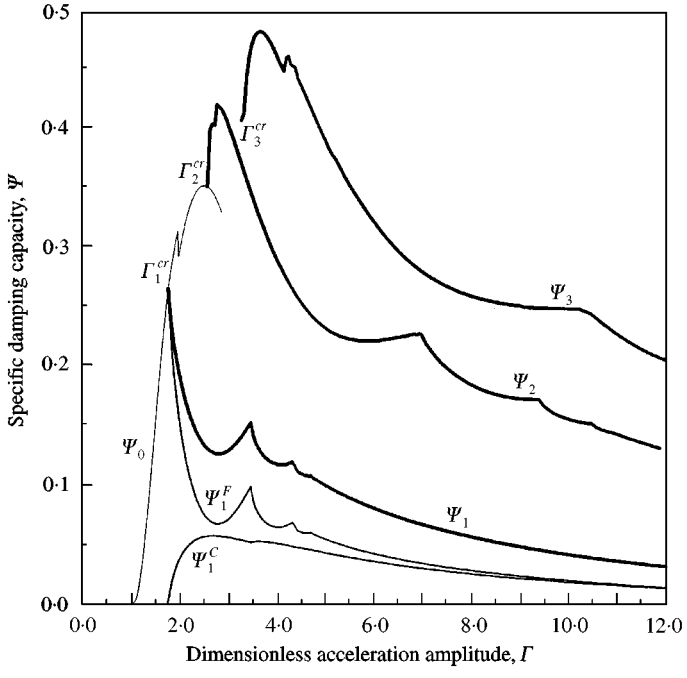


Figure 14. Damping versus $\Gamma$ for three clearances: $\Psi_1$, $\Psi_2$, $\Psi_3$ correspond to $\Delta_1$, $\Delta_2$, and $\Delta_3$, respectively. $R = 0{\cdot}4$. ——, total damping; – – –, individual contributions to $\Psi_1$ from ceiling and floor; ——, $\Psi_0$, no ceiling.

### 5.3. PID AT HIGH VALUES OF $\alpha$

Next, we examine the asymptotic behavior of $\Psi$ in the limit as $\Gamma$ becomes very large compared to $\Gamma_j^{cr}$. In Figures 13(a)–13(d), $\Delta$ is held constant at $\Delta_1 = 1{\cdot}62$ ($\Gamma_1^{cr} = 1{\cdot}75$), whereas $\Gamma$ varies from 1·5 to 12. In Figures 13(a) and 13(b) where $\Gamma \leqslant \Gamma_1^{cr}$ and in Figure 13(c) where $\Gamma$ is slightly greater than $\Gamma_1^{cr}$, the acceleration of gravity greatly influences the motion of the particle. However, in Figure 13(d), where $\Gamma = 12$, the decrease in the velocity of the particle between impacts is negligibly small compared to its "launch velocity", $v_s$. Therefore, without introducing an appreciable error, we can ignore the effect of gravity on the motion of the particle as well as the primary mass. An immediate consequence of this assumption is that $v_p =$ constant between impacts. Then $g$ drops out of the list of independent variables in equation (18), the number of dimensionless variables decreases from four to three, and equation (19) reduced to $\Psi = f(\mu, \alpha; R)$. Since $\mu$ is fixed in our experiments, and assuming that $R$ is a constant, $\Psi$ may be viewed as a function of a single variable $\alpha = U/d$ (or $\alpha = \Gamma/\Delta$).

In order to test the validity of this assumption, we combine the *first cycle* damping in Figure 6 for $\Gamma \geqslant \Gamma_j^{cr}$, $\Delta_j$, $j = 1, 2, 3$, and plot it against $\alpha = \Gamma/\Delta$; this is shown in Figure 17. (When the results were plotted on a linear scale, the curves were extremely cluttered at small $\alpha$; hence the use of the log-linear plot.) It is remarkable that three distinct sets of data collapse into a single set during the transformation from $\Psi(\Gamma, \Delta)$ to $\Psi(\Gamma/\Delta)$ over a rather large range of $\Gamma$ and $\Delta$. Next, we take the analytical results in Figure 15 for $\Gamma \geqslant \Gamma_j^{cr}$, $\Delta_j$, $j = 1,2,3$ and re-plot it as a function of $\alpha$ in Figure 17. The three curves, indicated by thin solid lines, become very close to each other, and are virtually indistinguishable for $\alpha > 3$.

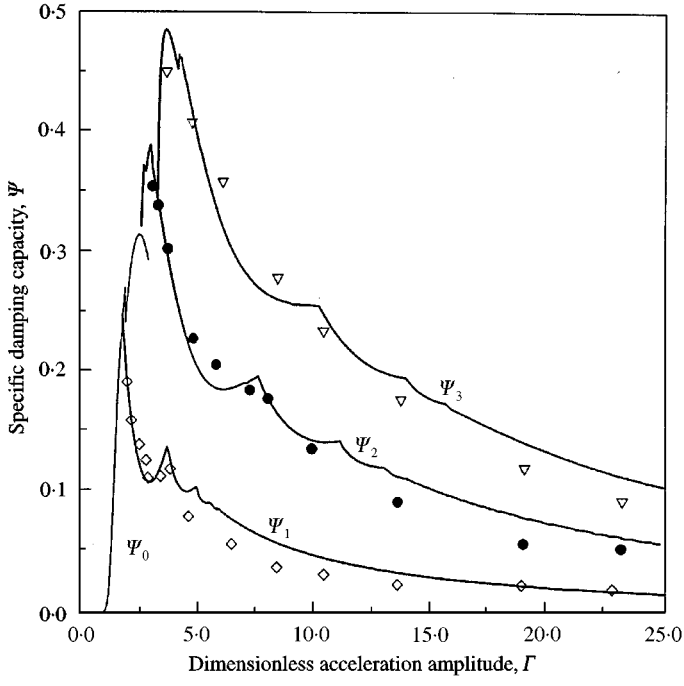


Figure 15. Comparison of theoretical damping to experimental results for three clearances: ——, $\Psi_1$, $\Psi_2$, and $\Psi_3$ correspond to $\Delta_1$, $\Delta_2$, and $\Delta_3$ respectively; ——, $\Psi_0$, no ceiling; ◇, $\Delta_1 = 1{\cdot}62$, best fit $R = 0{\cdot}48$; ●, $\Delta_2 = 4{\cdot}87$, best fit $R = 0{\cdot}48$; ▽, $\Delta_3 = 8{\cdot}11$, best fit $R = 0{\cdot}39$

We conclude that our assumption–that the effects of gravity may be neglected for a sufficiently high $\alpha$—appears to be well justified for $\alpha > 3$.

Encouraged by this observation, we now construct an even simpler model for predicting $\Psi$ when $\alpha$ is large. In the absence of gravity, the separation displacement, $u_s = 0$. The moment of separation then becomes $\omega_1 t_s = \pi/2$. If we measure the normalized time from the moment of separation, $\theta \equiv (\omega_1 t - \pi/2)$, then the moment of the first impact with the ceiling, $\theta_1$, depends only on $\alpha$ and is given by the simple transcendental equation

$$\theta_1 - \sin\theta_1 = \alpha^{-1}. \tag{34}$$

By examining the contribution to $\Psi$ from all of the impacts with the ceiling separately, it was found that the first impact damping, $\Psi_0^{FID}$, accounts for a large part of the total damping during the first half cycle. (See equation (33) and the discussion that follows.) In an effort to keep the model simple, we now ignore the successive impacts with the ceiling and "fold" the energy dissipated during these impacts into the effective coefficient of restitution, $R$. In Figure 13(d), after the particle comes to a relative rest against the ceiling of the primary mass, the particle is launched for the second time during the cycle. In the absence of gravity, this separation occurs when the primary mass crosses the position $u_2 = 0$. The motion in the second half of the cycle is antisymmetric with respect to the motion in the first half, and the contribution to $\Psi$ from the floor, $\Psi^F$, equals to that of the ceiling. This can be see graphically in Figure 14: as $\Gamma$ increases, the $\Psi^C$ and $\Psi^F$ approach each other. It follows that

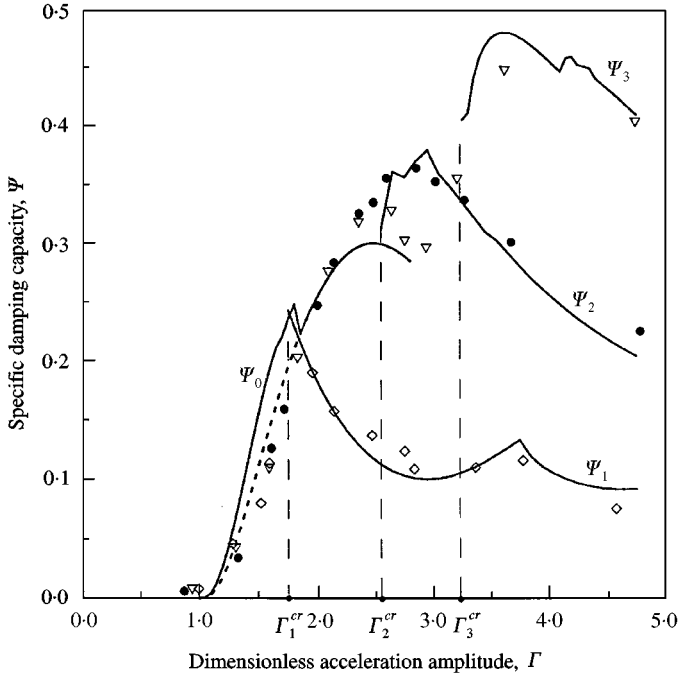


Figure 16. Comparison of theoretical damping to experimental results near $\Gamma^{cr}$: ——, $\Psi_1$, $\Psi_2$, and $\Psi_3$ correspond to $\Delta_1$, $\Delta_2$, and $\Delta_3$ respectively; ·····, $\Psi_0^{FID}$; ◇, $\Delta_1 = 1{\cdot}62$; ●, $\Delta_2 = 4{\cdot}87$; ▽, $\Delta_3 = 8{\cdot}11$.

the total $\Psi = 2\Psi^C$. From equations (9) and (13) we obtain

$$\Psi = 2(1 - R^2)\,\frac{\mu}{(1+\mu)^2}\,(1 - \cos\theta_1)^2, \tag{35}$$

where $\theta_1$ is the moment of the first impact with the ceiling given in terms of $\alpha$ in equation (34).

Predictions of equation (35) for $R = 0{\cdot}48$ (same as in the exact calculations) are plotted as the thick solid line in Figure 17. The comparison between the high $\alpha$ model and the exact theory is considered to be very good. Therefore, the exact analysis can be adequately approximated by equation (35) for $\alpha > 3$. For the design of a new particle impact damper. the high $\alpha$ model may be used to obtain a "quick" but fairly reasonable estimate of $\Psi$.

In Figure 17, as $\alpha$ increases, $\Psi$ asymptotically approaches zero. We offer a physically appealing explanation for this observation. At very high $\alpha$, after the particle separates from the floor of the primary mass, it is very quickly transferred to the ceiling. The particle velocity remains nearly constant, and the primary mass has not had time to decelerate appreciably. This results in a normalized impact velocity, $v_r^-$, that is very small (a very "soft" impact occurs). The damping, which is proportional to the *square* of $v_r^-$, is also very small. This process repeats itself during the second half of the cycle.

## 6. CONCLUSION

Traditionally, attempts to increase damping have largely focussed on the dissipation of the *stored elastic energy* in the structure. In this work, we take a different approach by

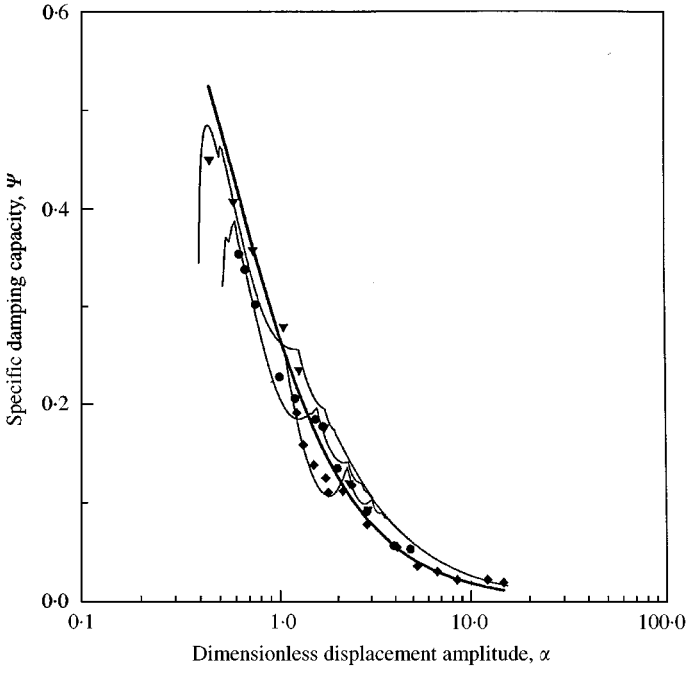


Figure 17. Comparison of theoretical damping to experimental results as a function of dimensionless displacement amplitude. $R = 0{\cdot}48$. ——, high $\alpha$ model (equation (35)); ——, exact solution (equations (13) and (17)); ◆, $\Delta_1 = 1{\cdot}62$; ●, $\Delta_2 = 4{\cdot}87$; ▼, $\Delta_3 = 8{\cdot}11$.

focusing on the dissipation of the *kinetic energy*. It is shown that, by the method of particle impact damping, a very high value of specific damping capacity ($\Psi \approx 50\%$) can be achieved for a very small weight penalty ($\beta \approx 6\%$). The damping was found to be highly non-linear, i.e., amplitude dependent. Therefore, a model of the damping was constructed that allows us to calculate cycle by cycle damping. In spite of the simplicity of the model, the comparison between theory and experiment was found to be remarkably good.

## REFERENCES

1. A. Papalou and S. F. Masri 1996 *Earthquake Engineering and Structural Dynamics* **25**, 253–267. Response of impact dampers with granular materials under random excitation.
2. C. Cempel and G. Lotz 1993 *Journal of Structural Engineering* **119**, 2642–2652. Efficiency of vibrational energy dissipation by moving shot.
3. N. Popplewell and S. E. Semergicil 1989 *Journal of Sound and Vibration* **133**, 193–223. Performance of the bean bag impact damper for a sinusoidal external force.
4. H. V. Panossian 1991 *Machinery Dynamics and Element Vibrations* **ASME DE-36**, 17–20. Nonobstructive particle damping (NOPD) performance under compaction forces.
5. H. V. Panossian 1992 *Journal of Vibration and Acoustics* **114**, 101–105. Structural damping enhancement via non-obstructive particle damping technique.
6. G. G. Wren and V. K. Kinra 1989 *Experimental Mechanics* **29**, 336–341. On the effect of an end-mass on beam damping.
7. D. J. Gorman 1975 *Free Vibration Analysis of Beams and Shafts*. New York: John Wiley.
8. G. Vertes 1985 *Structural Dynamics*: *Vol.* 11 *Developments in Civil Engineering*. Amsterdam: Elsevier.

## APPENDIX A: NOMENCLATURE

| | |
|---|---|
| $a$ | acceleration of the primary mass, $M$ |
| $c$ | reduced damping coefficient of the beam |
| $d$ | clearance of the enclosure |
| $g$ | acceleration due to gravity ($= 9{\cdot}81\ \mathrm{m/s^2}$) |
| $K$ | reduced stiffness of the beam |
| $L$ | length of the beam |
| $m$ | mass of the particles |
| $m_e$ | end mass of the beam |
| $m_{encl}$ | mass of the enclosure |
| $M$ | primary mass (reduced mass of the beam) |
| $M_b$ | mass of the beam |
| $R$ | effective coefficient of restitution |
| $T$ | maximum kinetic energy during a cycle |
| $\Delta T$ | kinetic energy converted into heat during one cycle |
| $u$ | displacement of the primary mass, $M$ |
| $u_p$ | displacement of the particle mass, $m$ |
| $u_s$ | displacement at which particles separate from floor |
| $U$ | displacement amplitude of the primary mass |
| $v$ | velocity of the primary mass, $M$ |
| $v_p$ | velocity of the particle mass, $m$ |
| $v_r^-$ | dimensionless relative impact velocity just prior to impact |
| $v_s$ | velocity at which particles separate from floor (launch velocity) |
| $V$ | velocity amplitude of the primary mass |
| $\alpha$ | dimensionless displacement amplitude ($= U/d$) |
| $\Delta$ | dimensionless clearance, ($= d\omega_1^2/g$) |
| $(\Delta^{cr}, \Gamma^{cr})$ | $(\Delta, \Gamma)$ which satisfy the osculation condition |
| $\beta$ | weight penalty, ($= m/M_b$) |
| $\phi$ | fundamental mode shape of the beam |
| $\gamma$ | mass per unit length of the beam |
| $\Gamma$ | dimensionless acceleration amplitude ($= U\omega_1^2/g$) |
| $\Gamma_0^A$ | amplitude above which particles are no longer in contact with the primary mass at the end of the first cycle |
| $\Gamma_0^B$ | amplitude above which only a single impact occurs in the first cycle |
| $\mu$ | mass ratio ($= m/M_2$) |
| $\tau$ | dimensionless time |
| $\omega$ | undamped circular natural frequency |
| $\psi_b$ | specific damping capacity of beam material |
| $\Psi$ | specific damping capacity |
| $\Psi_0^{FID}$ | damping due to first impact only |
| $\zeta$ | damping ratio |